A&A 601, A68 (2017)
DOI: 10.1051/0004-6361/201630267

Astronomy & Astrophysics

Deep into the Water Fountains

The case of IRAS 18043−2116

A. F. Pérez-Sánchez[1,2], D. Tafoya[3], R. García López[4], W. Vlemmings[3], and L. F. Rodríguez[2]

[1] European Southern Observatory, Alonso de Córdova 3107, Vitacura, Casilla 19001, Santiago, Chile
e-mail: aperezsa@eso.org
[2] Instituto de Radioastronomía y Astrofísica, UNAM, Apdo. Postal 3-72 (Xangari) 58089 Morelia, Michoacán, Mexico
[3] Department of Earth and Space Sciences, Chalmers University of Technology, Onsala Space Observatory, 439 92 Onsala, Sweden
[4] Dublin Institute for Advanced Studies, 31 Fitzwilliam Place, Dublin 2, Ireland

Received 16 December 2016/ Accepted 15 February 2017

ABSTRACT

Context. The formation of large-scale (hundreds to a few thousands of AU) bipolar structures in the circumstellar envelopes (CSEs) of post-asymptotic giant branch (post-AGB) stars is poorly understood. The shape of these structures, which is traced by emission from fast molecular outflows, suggests that the dynamics at the innermost regions of these CSEs does not depend only on the energy of the radiation field of the central star.
Aims. Multi-frequency observations toward a group of post-AGB sources known as Water Fountain (WF) nebulae can help to constrain the nature of the mechanism responsible for the launching and collimation of the fast molecular outlflows traced by high-velocity features of H_2O maser emission.
Methods. Deep into the WFs is an observational project based on the results of programs carried out with three telescope facilities: the *Karl G. Jansky* Very Large Array (JVLA), the Australia Telescope Compact Array (ATCA), and the Very Large Telescope (SINFONI-VLT).
Results. Here we report the results of the observations toward the WF nebula IRAS 18043−2116: detection of radio continuum emission in the frequency range 1.5–8.0 GHz, H_2O maser spectral features and radio continuum emission detected at 22 GHz, and H_2 ro-vibrational emission lines detected at the near infrared.
Conclusions. The high-velocity H_2O maser spectral features and the shock-excited H_2 emission could be produced in molecular layers that are swept up as a consequence of the propagation of a jet-driven wind. Using the derived H_2 column density, we estimated a molecular mass-loss rate on the order of 10^{-9} $M_\odot$ yr^{-1}. On the other hand, if the radio continuum flux is generated as a consequence of the propagation of a thermal radio jet, the mass-loss rate associated with the outflowing ionized material is on the order of 10^{-5} $M_\odot$ yr^{-1}. A rotating disk could be a plausible explanation for the mass-loss rates we estimated.

Key words. stars: AGB and post-AGB – circumstellar matter – stars: winds, outflows – infrared: stars – radio continuum: stars – masers

1. Introduction

Water Fountain (WF) nebulae are thought to represent a subclass of axisymmetric post-asymptotic giant branch (post-AGB) stars whose collimated outflows are traced by high-velocity (>100 km s^{-1}) 22 GHz H_2O maser spectral features. The first WF nebulae was reported by Likkel & Morris (1988). Results from interferometric observations toward the circumstellar envelopes (CSEs) of WFs indicate that, in most cases, the spatial distribution of the detected H_2O maser components (projected on the plane of the sky) can be correlated with large-scale bipolar structures (e.g., Sahai et al. 2005b; Vlemmings et al. 2006; Gómez et al. 2011; Lagadec et al. 2011; Yung et al. 2011).

The pumping of the H_2O maser transitions that trace high-velocity molecular outflows is thought to be dominated by shocks with neutral molecular gas (Hollenbach et al. 2013; Gray et al. 2016). The pumping mechanism of the H_2O transitions is very sensitive to changes of the collisional rates and requires particular conditions of the density and kinetic temperature of the gas (e.g., Humphreys 2007, and references therein). The detection of high-velocity spectral features of H_2O masers indicates that there are molecular layers in the bipolar structures where this particular set of physical conditions is met. Given the velocity of the spectral features, the dynamics of these layers might be a consequence of the passage of a high-velocity outflow throughout the slower and relic AGB wind.

Observational tools such as molecular H_2 emission at near-infrared wavelengths, radio continuum emission, and both hydroxyl (OH) and H_2O maser emission have been used in order to trace the actions of shocks, magnetic fields, and ionized shells on large-scale bipolar structures observed toward post-AGB stars (Sahai et al. 2005a; Cerrigone et al. 2008, 2011; Walsh et al. 2009; Bains et al. 2009; Lagadec et al. 2011; Gledhill & Forde 2012, 2015; Pérez-Sánchez et al. 2013; Tafoya et al. 2014; Gonidakis et al. 2014). In the context of the evolution of the CSEs of late-type stars, multi-frequency observational studies of WF nebulae provide important information regarding the physics behind the shapes of the bipolar structures that are observed toward more evolved counterparts. In particular, the momentum measured toward bipolar molecular outflows of a sample of 32 post-AGB (or protoplanetary nebulae) stars by Bujarrabal et al. (2001) indicates the necessity of an additional

energy source (besides radiation pressure) in order to explain the high-velocity components of the CO emission detected toward these sources. However, the nature of such energy source(s) as well as the parameters related to the high-velocity outflows (wind velocity, mass in the outflow, magnetic field strength, etc.) are yet to be determined.

2. Framework

2.1. H_2 ro-vibrational lines

Integral field spectroscopy at near infrared (near-IR) wavelength bands is useful to trace the activity at the innermost region of bipolar post-AGB sources, for instance, by the detection of molecular hydrogen (H_2) emission (e.g., Forde & Gledhill 2012). Moreover, the main excitation mechanism of the H_2 ro-vibrational lines, either UV-pumped or shock-excited, can be constrained using the flux ratios of the detected H_2 spectral features. In particular, *K*-band integral field spectroscopy has yielded important results toward late-type sources at different evolutionary stages, from those young post-AGB sources ($T_{\rm eff} < 1.5 \times 10^4$ K) that are not hot enough to photoionize the innermost layers of their CSEs (Sánchez Contreras et al. 2008; Gledhill & Forde 2012), to the so-called "hot post-AGB" sources, which are detected in both near-IR (Gledhill & Forde 2015) and radio wavelengths (Cerrigone et al. 2008, 2011).

In the shock-excited scenario, the populations of the H_2 ro-vibrational levels depends primarily on the strength of a passing shock-front, and also on the density of the pre-shock region. In this case, the population of the low-vibrational H_2 levels is favored over that of high-vibrational states. Indeed, the flux density ratio of the H_2 ro-vibrational lines 1–0 S(1)/2–1 S(1) $\geq$ 10 (although values >4 are also considered, Shull & Hollenbach 1978), is commonly used as a reliable diagnostic of shock-excited H_2 emission.

In the radiative scenario, the absorption of Lyman or Werner photons by the H_2 molecule leads to a cascade from high- to low-vibrational states via H_2 ro-vibrational transitions (fluorescence). Hence, UV-pumped emission eventually leads to the population of the low- and high-vibrational H_2 states. In the UV-pumped scenario, the near infrared spectra display both low- and high-vibrational H_2 ro-vibrational lines, as well as the Brγ and the He I recombination lines, with most of these high-energy lines displaying spatially extended emission. These lines in particular trace regions with a high degree of ionization, which in turn are associated with the strong radiation field of an early-B central star. In the case of WF nebulae, results of near-IR integral field spectroscopy toward the WF nebulae IRAS 16342−3814 were reported by Gledhill & Forde (2012). The authors showed that the spatially resolved H_2 emission traces high-velocity molecular outflows instead of UV-pumped shells. The non-detection of the Brγ emission line or He I recombination lines in this spectral window, together with a measured integrated flux ratio H_2 1–0 S(1)/2–1 S(1) > 10, supported a shock-excited scenario for the emission.

2.2. Radio continuum and the spectral energy distribution

At centimeter radio wavelenghts, the contribution from cold CSE dust and molecular gas is negligible. The flux detected at radio frequencies is usually associated with free-free interactions in energetic winds (Reynolds 1986). The study of the spectral energy distribution (SED) at radio wavelengths can help to constrain the nature of the continuum emission at frequencies where it is expected to be dominated by free electrons (either thermal or non-thermal emission). The spectral index of the SED and the frequency where the emission becomes optically thin provides information about the density and the temperature distribution of the emitting particles. For instance, Bains et al. (2009) reported the detection of radio continuum emission toward three post-AGB sources. Of these, the SED measured toward WF IRAS 15445−5449 was found to display a steep negative spectral index between ≈5 GHz and ≈8.7 GHz. Pérez-Sánchez et al. (2013) confirmed that the non-thermal emission is arising from a synchrotron jet, spatially resolved at 22 GHz.

2.3. IRAS 18043−2116

The WF IRAS 18043−2116 is one of the three hot WF nebulae detected to display 321 GHz H_2O maser emission (Tafoya et al. 2014). Sevenster & Chapman (2001) reported on the detection of only one of the two OH main-line transitions (1665 MHz), and both OH satellite lines (1612 and 1720 MHz) toward this WF source. Indeed, the detection of the 1720 MHz OH maser line is usually associated with shocks and interacting winds (Deacon et al. 2004, and references therein).

Based on its position on the MSX and IRAS two-color diagrams and on the line profile of the OH maser lines, Sevenster & Chapman (2001) associated the emission with an evolved star, most likely a post-AGB source. Deacon et al. (2004) reported on the redetection of the OH maser lines reported by Sevenster & Chapman (2001), and confirmed the non-detection of the 1667 MHz OH maser line. The blue- and redshifted spectral features of the double-peaked 1665 MHz OH maser spectrum were detected at 69.7 km s^{-1} and 104 km s^{-1}, respectively. Based on the velocity of the 1665 MHz OH maser spectral features, the authors therefore suggested a radial velocity for the stellar source of 87.5 km s^{-1}.

Deacon et al. (2007) reported the detection of high-velocity 22 GHz H_2O maser emission, whose spectral features had velocities beyond the velocity range defined by the double-peaked 1665 MHz OH maser spectrum ($\Delta v = v_{\rm red} - v_{\rm blue} \approx 33$ km s^{-1}, Deacon et al. 2004). This led the authors to classify the source as a WF nebulae. Gonidakis et al. (2014) reported the detection of linear and circular polarization of the OH 1665 MHz maser spectral features. The percentage of circular polarization detected in the strongest spectral feature was 52%, which the authors associated with the σ-components of Zeeman splitting of this maser spectral line, and consequently, with the action of a magnetic field.

In addition to the detection of 321 GHz H_2O maser emission (Tafoya et al. 2014), Pérez-Sánchez et al. (2011) and Walsh et al. (2009, 2014) also reported the detection of the 22 GHz H_2O maser transition. In most cases the bandwidth used for the observations led to the detection of maser spectral features over velocity ranges >300 km s^{-1}, which confirmed the results reported by Deacon et al. (2007).

Here we report the first detection of radio continuum emission in the frequency range between 1.0 GHz and 8.0 GHz using the *Karl G. Jansky* Very Large Array (JVLA) toward the WF IRAS 18043−2116. We also report the detection of the S- and Q-branch H_2 ro-vibrational lines using SINFONI/VLT for the first time toward this source. In addition, the result from 2013 observations made using the Australia Telescope Compact Array (ATCA) of maser and radio continuum emission at 22 GHz is also presented.

3. Observations

3.1. JVLA data

The observing program (project code: 15A-301) was executed between June and August 2015, using the most extended (A) configuration of the JVLA, in frequency bands *L*, *S*, and *C*. The scheduling blocks were arranged by frequency band. Each block included 11 science sources and their respective flux and phase calibrators. In this paper we concentrate on the emission detected toward the WF IRAS 18043−2116. The report on the results for the entire sample of targets will be published in a separate paper.

Each frequency band was observed once during two days, producing two different data sets of visibilities for each band. Each data set was calibrated independently. However, the two data sets that belong to the same frequency band were eventually combined during the deconvolution process. An initial calibration of the data was performed using the VLA CASA calibration pipeline. Then, the visibilities were split by source (science and calibrators) in order to continue the calibration process (when necessary), or to start the image deconvolution process.

In the case of WF IRAS 18043−2116, the good signal-to-noise ratio ($S/N \approx 60$) within the frequency bands *S* and *C* allowed us to calculate the intensity maps using the multi-frequency synthesis algorithm (mfs) mode for wide frequency bands. In our case, the continuum images were calculated over effective bandwidths of ≈1.73 GHz (*S* band) and ≈1.75 GHz (*C* band). In addition, an image of each spectral window was deconvolved in order to measure the flux and retrieve the spectral energy distribution within the two frequency bands (see Table 1). On the other hand, the resulting bandwidth at frequency band *L* is ≈800 MHz. The deconvolution process was performed using the mfs mode, but because of the low S/N, it was not possible to deconvolve reliable maps of individual spectral windows within this frequency band.

Table 1. Radio continuum fluxes toward the WF IRAS 18043−2116.

Frequency (MHz)	Intensity (mJy)				Beam (arcsec^2)
	2.0 GHz band		0.1 GHz spw		
	S_ν	rms	S_ν	rms	
1498.994	0.335	0.093			3.60 × 0.96
2051.006			0.570	0.201	1.54 × 0.82
2435.007			0.737	0.155	1.34 × 0.70
2563.008			0.604	0.122	1.26 × 0.66
2691.008			0.865	0.128	1.21 × 0.62
2819.008			0.627	0.104	1.17 × 0.60
2947.009			0.705	0.112	1.11 × 0.58
2999.012	0.708	0.036			0.93 × 0.48
3051.009			0.640	0.095	1.11 × 0.56
3179.009			0.738	0.084	1.07 × 0.55
3307.010			0.705	0.084	1.02 × 0.53
3435.010			0.818	0.084	0.98 × 0.51
3563.011			0.658	0.071	0.96 × 0.49
3819.011			0.826	0.108	0.88 × 0.45
3947.012			0.671	0.102	0.88 × 0.45
4551.006			0.839	0.114	0.71 × 0.39
4807.006			0.793	0.106	0.69 × 0.38
4935.006			0.690	0.102	0.66 × 0.36
5063.007			0.759	0.100	0.64 × 0.35
5191.007			0.758	0.095	0.63 × 0.34
5319.007			0.912	0.106	0.61 × 0.33
5447.007			1.026	0.121	0.60 × 0.33
5499.008	0.922	0.030			0.54 × 0.30
5551.007			0.989	0.134	0.58 × 0.32
5679.007			0.893	0.106	0.58 × 0.31
5807.008			0.862	0.111	0.57 × 0.31
5935.008			0.813	0.100	0.54 × 0.30
6063.008			0.866	0.107	0.52 × 0.30
6191.008			0.991	0.170	0.47 × 0.28
6319.008			0.887	0.110	0.50 × 0.28
6447.008			0.763	0.100	0.49 × 0.29
22 227.259	0.705	0.095			3.0 × 0.53

3.2. ATCA data

Previous observations toward IRAS 18043−2116 were carried out using ATCA in 2013 at 22.2 GHz (project code: CX267, director's discretionary time). A bandwidth of 2 GHz centered on the rest frequency 22.235 GHz was used for the Compact Array Broadband Backend (CABB), this using the 32 × 64 MHz mode. This setup allowed the implementation of three overlapped zoom bands (three 64 MHz channels with 2048 channels each) centered on the rest frequency 22.235 GHz, covering 128 MHz for the maser emission observations (a velocity range of 1725.8 km s^{-1}). The final spectral resolution for the line observations was 0.42 km s^{-1}. The radio continuum was simultaneously observed using the remaining bandwidth of 1.8 GHz.

The observing program was executed using the most extended configuration of the ATCA array (6A). The shortest baseline length of this configuration is 337 m (for comparison, the shortest baseline of the A configuration of the JVLA is 680 m). The calibration of the ATCA continuum data was made using the radio interferometry data reduction package MIRIAD (Sault et al. 1995). It was also used to calibrate and restore the H_2O maser spatial distribution projected on the plane of the sky. First, the spectral channel with the highest S/N value of the H_2O maser spectra was self-calibrated. Then, the solution tables were copied to the two visibility sets, the continuum and the maser visibilities. This allowed us to determine the relative positions between the H_2O maser spectral features and the peak of the radio continuum. In order to determine the projected spatial distribution of the maser emission, the AIPS task SAD was used on each individual channel of the H_2O maser data cube. When the channels with maser emission were identified, the spatial distribution of the emission on the plane of the sky was determined.

3.3. SINFONI (VLT) data

The WF IRAS 18043−2116 was observed with the Very Large Telescope at Paranal Observatory, Chile, using the *K*-band grating of the SINFONI integral field spectrograph installed at the 8.2 m UT4 (Eisenhauer et al. 2003; Bonnet et al. 2004). The source was observed on 2015 May 10, covering the wavelength range 1.95–2.45 μm with spectral resolution ≈4000, using the no optics guide star (noAO) mode. The pixel scale was 250 mas which corresponds to a field of view of 8″ × 8″. The seeing during the observations was ∼0.8 arcsec. The total integration time was 4200 s. Dark, bad-pixel mask, flat-fielding, optical distortion corrections, and wavelength calibration were performed using the SINFONI data-reduction pipeline. In order to correct the spectra for the atmospheric transmission, absorption features, and to flux-calibrate the final datacube, a telluric standard star of spectral type B3V was observed. The telluric standard data were reduced in the same way as the science source data. The standard

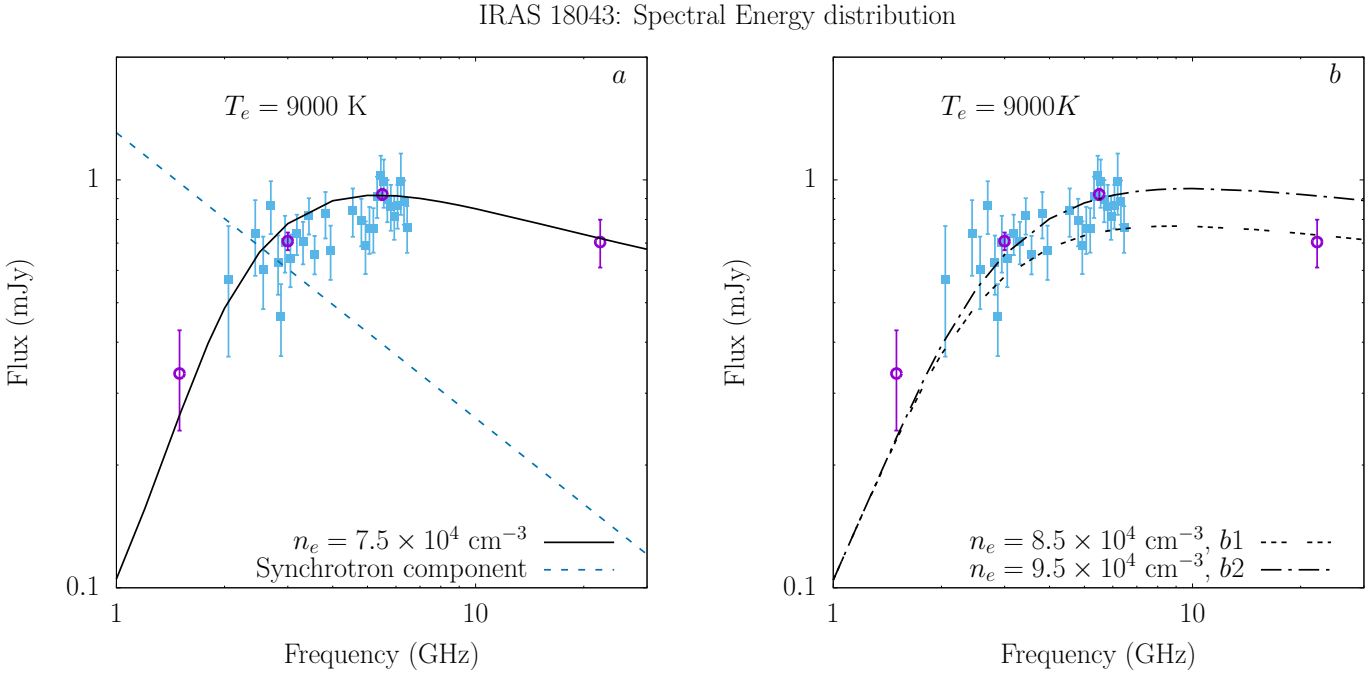

Fig. 1. Spectral energy distribution measured toward the WF IRAS 18043−2116. The small filled squares are the measurements at individual spectral windows within JVLA frequency bands *C* and *S*. The open circles represent the fluxes obtained from mfs evaluated at the central frequency of JVLA bands *L*, *S*, and *C*. The flux at 22 GHz was measured in 2013 with ATCA. The different lines in the panels represent the fit to the data points obtained from radiative transfer of radio continuum emission (see text). In panel **a)** the model includes thermal and nonthermal components, assuming the latter is synchrotron radiation with flux at 22 GHz of 0.15 mJy and spectral index =−0.7 (dashed line). At low frequencies the synchrotron component is mostly absorbed by optically thick free-free emission and does not contribute to the total emission. In panel **b)**, the models only consider thermal emission. Model *b*1 fits the flux at 22 GHz measured with ATCA in 2013, whereas Model *b*2 fits the fluxes measured with JVLA in 2015. The difference between the two thermal models suggests an increase in the 22 GHz flux density of ≈20% between 2013 and 2015.

star spectrum was extracted from the datacube by averaging the central spaxel spectra of the datacube down to the seeing size. The standard spectra was then divided by a blackbody at the appropriate temperature. This result was then employed to correct for the telluric features and atmospheric transmission after the intrinsic features of the standard spectrum were removed. Finally, the continuum-substracted images were constructed by running iteratively the IRAF subroutine CONTINUUM along the dispersion axis at each spatial position across the datacube. The final spaxel resolution in the spectral direction (channel) obtained is 2.45×10^{-4} μm (~34.6 km s^{-1}).

The SINFONI field-of-view (FoV) was centered on the infrared (IRAS) coordinates reported in the literature for IRAS 18043−2116 (J2000 $18^h7^m21.1^s$; $-21°16'14.2''$). However, the angular offset of the center of the SINFONI FoV with respect to the coordinates of the source retrieved from the JVLA and ATCA observations is ~3.95 arcsec. The absolute uncertainty on the position of SINFONI-VLT is 1″–2″, and the uncertainty on the position of the JVLA observations, as we did not observe using optimized phase-referencing calibrators, should be on the same order. With these uncertanties, the radio source and the source at the center of the SINFONI FoV cannot be associated. The coordinates of the radio source from our JVLA observations are (J2000)$18^h7^m20.853^s$; $-21°16'12.271''$. The closest source to this position within the SINFONI FoV has an angular offset of 1.82″. Although it is detected toward the edge of the SINFONI FoV, we assume that the emission detected toward this position is associated with our science target. A spectrum of this feature was extracted by averaging 3×3 pixels at the detected position along the dispersed axis.

4. Results

4.1. Radio continuum emission

The fluxes measured at the different spectral windows of frequency bands *L*, *S*, and *C* of the JVLA, and the flux measured with ATCA at 22 GHz are listed in Table 1. All the fluxes were obtained from fitting a two-dimensional Gaussian model to the (spatially unresolved) brightness distribution in the restored images using the AIPS task *JMFIT*. The uncertainty of the measurements correspond to the 1σ error of the Gaussian model. The SED is presented in Fig. 1. The flux measured within band *C* is higher than the fluxes measured in bands *S* and *L*, where the values of the flux density are ≈23% and ≈64% lower, respectively. Moreover, the flux measured with ATCA at 22 GHz in 2013 is ≈24% lower than the flux measured in band *C*. Although the source is not spatially resolved at centimeter wavelengths, it is worth noting that the extent of the shortest baseline of the ATCA 6A array configuration is about half the extent of the shortest baseline of the JVLA A configuration. This allows us to rule out the possibility of flux losses due to resolving out extended structures of the source at 22 GHz.

Overall, the SED of IRAS 18043−2116 resembles the radio continuum spectrum expected from stellar winds (Reynolds 1986). The shape of the SED indicates that the radio continuum emission is optically thick below ≈5.5 GHz, with slope $\alpha < +2$. Above 5.5 GHz the slope turns over into a flat, optically thin spectrum. Using the value of the flux measured with ATCA at 22 GHz to calculate the spectral index above the turnover frequency (ν_c = 5.5 GHz) we obtained $\alpha = -0.2 \pm 0.2$. This could suggest the presence of a nonthermal component

that significantly contributes to the radiation field. However, this value must be carefully considered as there is a gap of two years between the JVLA and the ATCA observations. Indeed, radio continua detected toward post-AGB stars have shown variability on timescales from a few to tens of years (Cerrigone et al. 2011). Nonetheless, the optically thin nature of the SED above 5.5 GHz can still be inferred from the fluxes measured at the high-frequency spectral windows within band *C* (see Fig. 1).

The main constraint on the interpretation of the data is the flux density measured at 22 GHz. As mentioned above, the flux at 22 GHz was measured two years before the JVLA observations, therefore it might have changed. In Fig. 1 we present two plausible scenarios based on the best fits of our data sample. In the first scenario (panel a) we assumed that the flux at 22 GHz did not change since the measurements of 2013. In this scenario we can fit the data with a model that considers both thermal and nonthermal components. For this model we use a synchrotron (nonthermal component) flux at 22 GHz of 0.15 mJy and spectral index $\alpha_s = -0.7$ (the dashed line in panel a). Moreover, in the model the synchrotron source is surrounded by a thermal electron sheath with density $n_e = 7.5 \times 10^4$ cm^{-3} and temperature $T_e = 9000$ K, which is responsible for the thermal component of the emission.

The second scenario is based on the variability of the flux density at 22 GHz. In this case we assume that the flux might have increased rather than decreased between 2013 and 2015. Although the latter cannot be ruled out, a lower flux density at 22 GHz in 2015 might imply a stronger synchrotron (nonthermal) component. In Fig. 1, panel b shows the results of the radiative transfer models including only thermal emission, assuming the source is an ionized shell. Model *b*1 (dotted line) is based on the flux density measured with ATCA at 22 GHz and therefore underestimates the fluxes measured in 2015 within the JVLA frequency bands. The electron density and temperature values obtained from the model are $n_e = 8.5 \times 10^4$ cm^{-3} and $T_e = 9000$ K.

Model *b*2 (dash-dotted line) is based on the fluxes measured with JVLA in 2015. The best fit indicates that the flux density at 22 GHz may have increased about 20% between 2013 and 2015. In this case, the electron density and temperature retrieved from the model are $n_e = 9.5 \times 10^4$ cm^{-3} and $T_e = 9000$ K. This means that the thermal emission models suggest that the electron density in the emitting region should have increased by ≈10% between 2013 and 2015. Nonetheless, both scenarios could be related to the propagation of a shock-front throughout a denser CSE (Cerrigone et al. 2011, and references therein).

4.2. High-velocity H_2O maser emission

Based on the spectral features of the 1665 MHz OH maser line, Deacon et al. (2004) suggested a systemic velocity for the stellar source of $v_{\star,\rm lsr} = 87.5$ km s^{-1} (dashed line in Fig. 2). The H_2O maser spectrum obtained with ATCA is presented in Fig. 2. The spectral features of the H_2O maser emission were detected spread over a velocity range of 400 km s^{-1}. We identified 33 H_2O maser spectral features that were color-coded as blue- and redshifted according to their velocity with respect to $v_{\star,\rm lsr}$. The extreme spectral features appear at LSR velocities of 349 km s^{-1} (redshifted) and −46 km s^{-1} (blueshifted). In total, the blueshifted emission covers a velocity range of 132 km s^{-1}, with the (blueshifted) brightest features moving at 20 km s^{-1} with respect to $v_{\star,\rm lsr}$. On the redshifted side, the spectral features are spread over a wider velocity range (264 km s^{-1}). The brightest maser spectral feature in the spectrum arises from the redshifted side, moving with velocity along the line of sight of 150 km s^{-1} with respect to $v_{\star,\rm lsr}$.

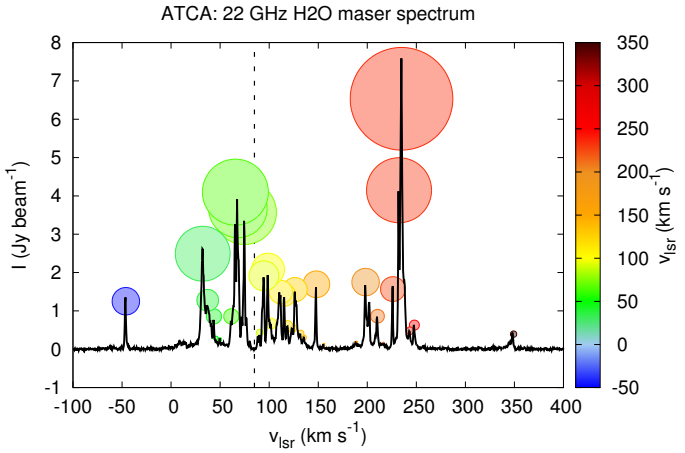

Fig. 2. 22 GHz H_2O maser spectrum detected toward the WF IRAS 18043−2116. The systemic velocity derived for the stellar source from the OH maser spectrum is $v_{\rm lsr,\star} = 87.5$ km s^{-1} (vertical dashed line, Deacon et al. 2004). The final spectral resolution is $\Delta v = 0.42$ km s^{-1}, and the total velocity range covered by the maser spectral features is 400 km s^{-1}.

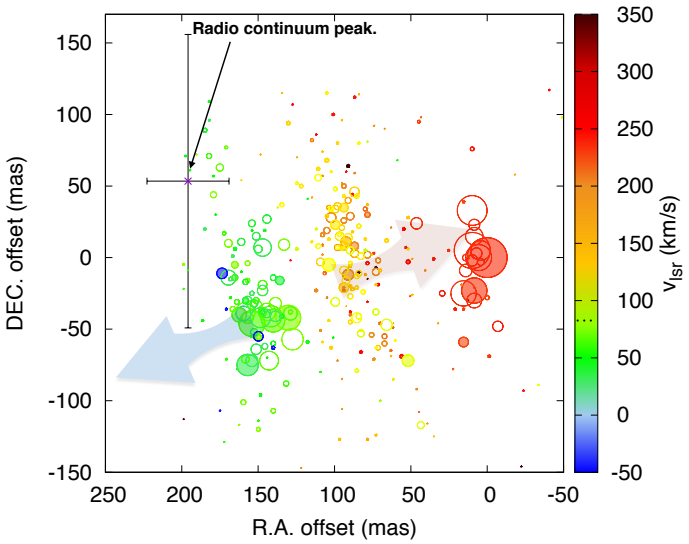

Fig. 3. Spatial distribution of the radio continuum and the spectral features of H_2O maser emission detected at 22 GHz with ATCA. The radio continuum and the H_2O maser observations were carried out simultaneously in 2013. The star with error bars shows the relative position of the peak of the radio continuum detected at 22 GHz with respect to the brightest H_2O maser feature. The size of each circle scales linearly with the intensity of emission measured in each channel related to H_2O spectral features. Each filled circle represents the brightest channel of each spectral figure in Fig. 2. The dots in the color bar indicate the velocity of the stellar source $v_{\star,\rm lsr}$. The blue and red arrows indicate a possible orientation (projected on the plane of the sky) of the axis defined by the high-velocity outflow traced by the H_2O maser emission.

The projected spatial distribution of the H_2O maser emission is presented in Fig. 3. The size of the circles scales as the peak intensity value measured at each individual channel. The offsets in this figure are given with respect to the position of the brightest spectral feature. The relative position of the radio continuum emission detected at 22 GHz is also shown in Fig. 3. The position uncertainty of the maser features is a function of the synthesized beam $\theta_{22\ \rm GHz}$ and of the S/N measured at each channel of the

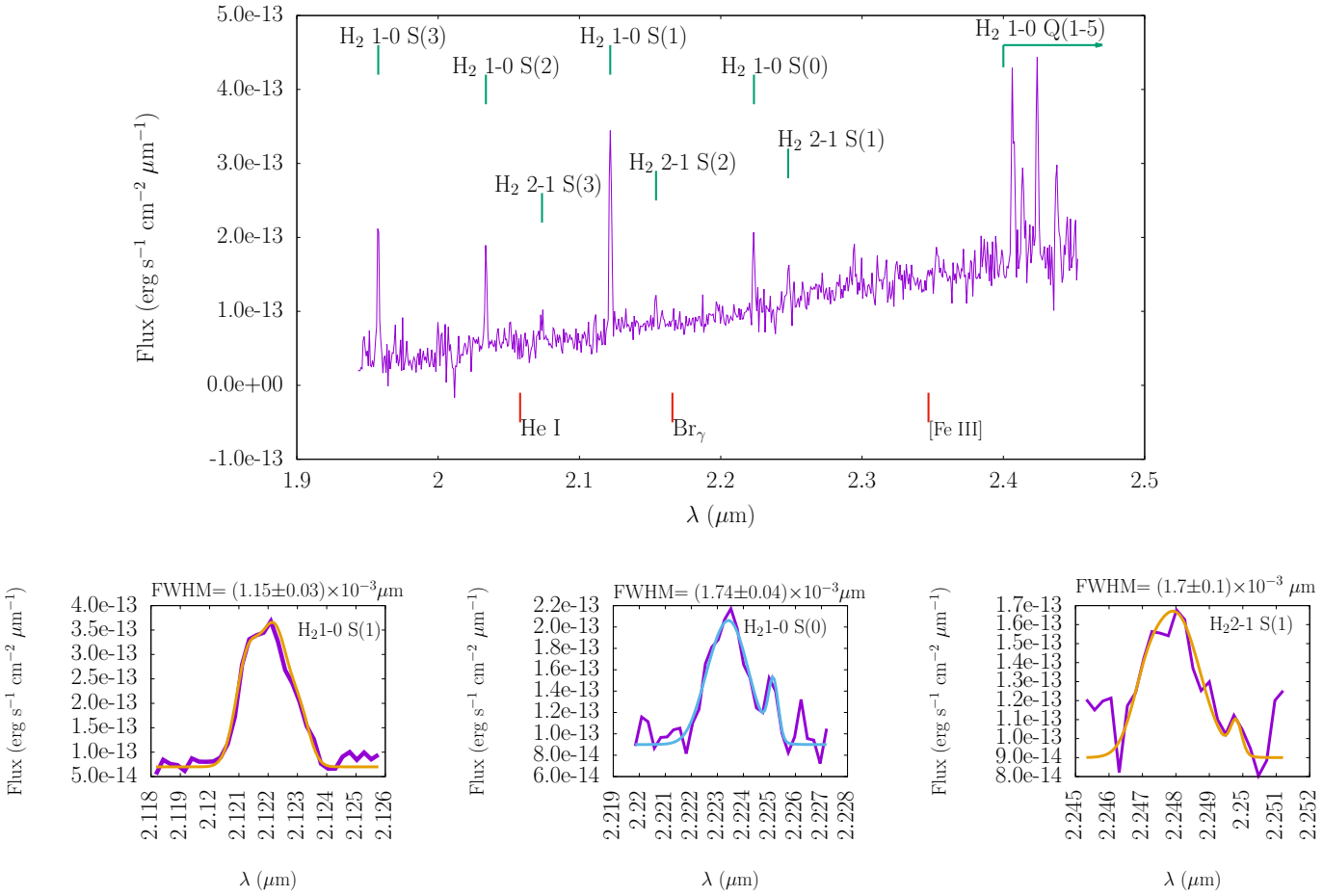

Fig. 4. SINFONI *K*-band spectrum detected toward the WF IRAS 18043−2116. The Q-branch and low-energy S-branch H_2 ro-vibrational transitions dominate the spectra. No energetic H_2 ro-vibrational lines were detected, neither Br_γ emission lines nor He recombination lines. The *bottom panels* display the ro-vibrational lines H_2 1–0 S(1), H_2 1–0 S(0), and H_2 2–1 S(1). A simple sum of two Gaussian functions was implemented to fit and then estimate the FWHM of each spectral feature.

spectrum; this is $\Delta\theta = 0.45\frac{\theta_{22\ \mathrm{GHz}}}{S/N}$ (Reid et al. 1988). The peak flux of the strongest and one of the weakest spectral features in Fig. 2 together with the rms value measured at the source position in a line-free channel (rms = 1.02×10^{-2} Jy/beam) were used in order to estimate the S/N. According to this, the minimum and maximum positional uncertainties along the major and minor axis of the synthesized beam for the maser observations (2.16″, 0.43″ and 18.37°) are 1.71 mas × 0.34 mas and 60 mas × 12 mas, respectively. Therefore, taking into account the positional error of the weak spectral features, all the H_2O maser features arise from within 180 × 200 mas^2 projected on the plane of the sky. The blue- and redshifted emission appear to arise from two separated groups. The spatial distribution of the blueshifted emission suggests that all the spectral features arise within the same line of sight. In turn, the redshifted emission is generated in two regions with angular separation of 90 mas from each other, both toward the east from the blueshifted emission. The projected position of the brightest maser spectral features suggests that it is generated in a region separated from the bulk of the redshifted emission.

4.3. SINFONI K-band integral field spectroscopy

The spectrum obtained with SINFONI (*K* band: 1.95–2.45 μm) is shown in Fig. 4. The spectral features detected correspond to the 1–0 Q(1–4)-branch as well as to low-vibrational S-branch lines. The fluxes measured in the different H_2 lines detected are listed in Table 2. No high-excitation lines such as He I recombination lines or the Brγ line were detected. The steep positive spectral index of the continuum baseline within the SINFONI *K* band is indicative of a reddened source, likely due to the presence of a dusty structure where the stellar source is still embedded.

The extinction can be estimated using the line flux ratio 1–0Q(3)/1–0S(1). Because the strength ratio of these transitions is intrinsic and fixed to their respective spontaneous decay rate

Table 2. H_2 ro-vibrational lines detected toward the WF IRAS 18043−2116.

Line	λ_0 (μm)	λ_p (μm)	F $\times 10^{-16}$ erg cm^{-2} s^{-1}	ΔF
1 0 S(3)	1.9575564	1.95749	5.45	0.23
1 0 S(1)	2.1218299	2.12199	6.22	0.14
2 1 S(2)	2.1542257	2.15393	0.75	0.097
1 0 S(0)	2.2233001	2.22343	2.15	0.24
2 1 S(1)	2.2477228	2.24783	1.06	0.23
1 0 Q(1)	2.4065935	2.40666	5.51	0.37
1 0 Q(2)	2.4134354	2.41376	3.38	0.53
1 0 Q(3)	2.4237289	2.42398	5.30	0.43
1 0 Q(4)	2.4374914	2.43769	4.56	1.11

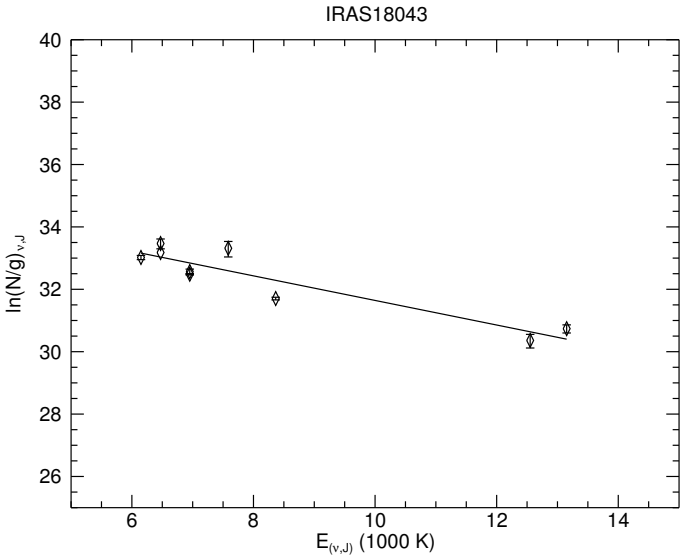

Fig. 5. H_2 rotational diagram relating the column density (N_{H_2}) of the upper level of the detected transitions with their respective excitation temperature in thermal equilibrium. The gas temperature estimated from the best fit to the data is $T_g = 2538 \pm 393$ K, and the estimated column density is $N_{H_2} = 2.348 \times 10^{-17}$ cm^{-2}.

ratio ($R_0 = 0.70$), any other value would be an indicator of extinction. From the fluxes in Table 2 we obtain 1–0Q(3)/1–0S(1) = 0.85 ± 0.01. Using the Rieke & Lebofsky (1985) extinction law, we estimated $A_V = 5$ mag. The ratio 1–0S(1)/2–1S(1) $\geq$ 4 is used as a reliable diagnostic of shock-excited H_2 emission (Shull & Hollenbach 1978). Using the fluxes in Table 2, we obtain 1–0(S1)/2–1(S1) = 5.86 ± 1.27. This value should increase if any line-of-sight extinction correction is applied to the fluxes measured. This fact supports the shock-excited origin of the ro-vibrational lines detected.

The FWHMs of most of the H_2 ro-vibrational lines detected are, on average, a factor of 5–6 larger than the final spectral resolution unit obtained in the SINFONI K band. In Fig. 4 we present the estimated FWHM for three low-vibrational lines of the spectrum. A simple one-dimensional Gaussian model was implemented to obtain standard dispersion and then to compute the $FWHM = 1.15 \times 10^{-3}, 1.69 \times 10^{-3}$, and 1.74×10^{-3} μm for the H_2 lines 1–0S(1), 1–0S(0), and 2–1S(1), respectively. The spectral resolution unit of our spectrum is $\Delta\lambda = 2.45 \times 10^{-4}$ μm ($\Delta v = 34.6$ km s^{-1}). Consequently, the velocity ranges defined by the blue and red wings of the spectral lines at the bottom in Fig. 4 are 163 km s^{-1}, 246 km s^{-1}, and 239 km s^{-1}, respectively. The line width of shock-excited H_2 ro-vibrational lines is a function of the inclination of the axis defined by the shock front with respect to the line of sight. The estimated velocity values agree with the velocities traced by the high-velocity spectral features of H_2O maser emission. However, high-spatial resolution observations are crucial for probing the spatial correlation between the gas traced by the high-velocity emission of H_2 and the gas traced by the high-velocity spectral features of H_2O maser emission.

The H_2 rotational diagram in Fig. 5 shows the logarithm of the column density ($N_{v,J}$) of the upper ro-vibrational state (divided by its statistical weight $g_{v,J}$) of the different H_2 transitions as a function of their excitation energy. Assuming thermal equilibrium, the slope of the best model fitting the data points is inversely proportional to the temperature of the molecular (H_2) gas. When we use the H_2 line fluxes measured, the column density of the emitting region is $N_{H_2} = 2.35 \times 10^{17}$ cm^{-2} and the estimated gas temperature is $T_g = 2538 \pm 393$ K. In particular, the temperature estimated from the H_2 rotational diagram agrees with the kinetic temperature of the gas required to generate not only the 22 GHz line, but also higher H_2O maser transitions such as the 321 GHz H_2O maser emission detected by Tafoya et al. (2014) toward this source.

5. Discussion

5.1. Spatial scale traced by the H_2O maser emission

The spatial distribution of the maser emission presented in Fig. 3 agrees with the results presented by Walsh et al. (2014). The overlap between the projected positions of the extreme velocity spectral features and the spectral features with LSR velocities close to $v_{\star,lsr}$, suggest that the gas traced by the H_2O maser emission propagates nearly along the line of sight (Walsh et al. 2009). Furthermore, the high-velocity range covered by the H_2 ro-vibrational lines and the H_2O maser spectral features indicates that the emission originates from molecular gas moving with velocities of hundreds of km s^{-1} with respect to $v_{\star,lsr}$.

The shock-excited ro-vibrational H_2 lines detected with SINFONI-VLT most likely trace the activity close to the region where the high-velocity winds are launched. Given that the main pumping mechanism of the H_2O maser transition is thought to be collisional, via neutral molecules such as H_2, a direct link could be drawn between the regions traced by the detected H_2 and H_2O spectral features. However, the H_2O maser emission might trace outer molecular layers along the high-velocity outflows where the inversion of the level population is not quenched by high collisional rates. When we assume that the molecular gas pumping the H_2O maser transition is driven by the high-velocity outflows and take into account the error in the position of the weak H_2O maser spectral features, the spatial distribution of the maser spectral features suggests that the mechanism driving the high-velocity outflow is one of the main (if not the most important) inputs of energy for the dynamics in regions with areas of a few thousand AU^2. New high angular resolution observations at near-IR and radio frequencies, improving the positioning of the source on the field of view at near-IR, could in principle probe the spatial distribution of the shock-excited ro-vibrational lines and the maser spectral features and thus confirm our interpretation.

5.2. Radio continuum flux: radio jet or HII region?

The relative position of the radio continuum peak detected with ATCA at 22 GHz is shown with respect to the brightest H_2O spectral feature in Fig. 3, and the nature of the source of the radio continuum emission can be inferred from the SED in Fig. 1. The SED indicates that the flux is dominated by a thermal component, with turnover frequency at 5.5 GHz. For reference, the SED from an idealized HII region (a homegeneous uniform isothermal ionized wind) results in $\alpha = +2$ in the optically thick regime, whereas above the turnover frequency, the emission becomes optically thin and $S_\nu \propto \nu^{-0.1}$ (e.g., Kurtz 2005, and references therein). In these cases the radio continuum is associated with Bremsstrahlung emission from the interaction of free electrons and ions in photoionized regions around hot ($T_{\rm eff} > 2.0 \times 10^4$ K) central radiation sources. The interpretation of the results of radiative transfer models presented in Fig. 1 depends on whether the flux density measured at 22 GHz remained stable during the period between 2013 and 2015. If the flux density did not

change, then our best model indicates that the radio continuum emission, although dominated by a thermal component, has a small but significant synchrotron (nonthermal) component with a flux density of 0.15 mJy at 22 GHz. This scenario implies a strong magnetic field that could be related to the collimation of the high-velocity outflow traced by the H_2O maser emission (e.g., Pérez-Sánchez et al. 2013). Nonetheless, new observations of radio continuum emission above 10 GHz are needed to probe the source of the nonthermal component.

When we assume that the flux density detected at 22 GHz has increased between 2013 and 2015, our best fits indicate that the source of the radio continuum might be Bremsstrahlung emission from thermal electrons. Our model suggests that an increase in electron density of ≈10% between 2013 and 2015 is needed to fit the SED measured from the JVLA data taken in 2015. Such an increase in electron density in the emitting region can be associated with the propagation of an ionizing shock front from the innermost region of the relic AGB CSE. We note that for both scenarios the models underestimate the flux density at lower frequencies, which suggests that the spectral index in the optically thick regime of the SED is $\alpha < +2$. Indeed, spectral index values $\alpha \leq +1.5$ in the optically thick regime and the gradual change of the slope near the turnover frequency are usually related to inhomogeneous (nonspherical), jet-like stellar winds (Reynolds 1986).

Using the velocity $v_{\star,\mathrm{lsr}}$ derived from the double-peak 1665 MHz OH maser spectra for the WF IRAS 18043−2116 (Deacon et al. 2004) and the revised kinematic distance calculator (Reid et al. 2009), we estimated the near and far kinematic distances: 6.2 ± 0.3 kpc and 10.4 ± 0.3 kpc, respectively. Hence, from the flux measured at the optically thin regime of the SED, the number of ionizing photons per second ($\dot{N}_\mathrm{i}$) needed in order to keep ionized the region detected in radio continuum can be estimated using the following relation (Schraml & Mezger 1969):

$$\dot{N}_\mathrm{i} = 8.9{\times}10^{43}\left(\frac{S_\nu}{\mathrm{mJy}}\right)\left(\frac{\nu}{4.9\ \mathrm{GHz}}\right)^{0.1}\left(\frac{D}{\mathrm{kpc}}\right)^{2}\left(\frac{T_{\mathrm{e}^-}}{10^4\ \mathrm{K}}\right)^{-0.45}\ \mathrm{s}^{-1}. \quad (1)$$

Then, with $S_{5.935\ \mathrm{GHz}} = 0.81$ mJy (see Table 1) in Eq. (1) and $T_\mathrm{e} = 9000$ K, we obtain $\dot{N}_\mathrm{i} = 8.37 \times 10^{45}\ \mathrm{s}^{-1}(D/10.4\ \mathrm{kpc})^2$. Despite the given dependence on the distance, the number of ionizing photons per second calculated is on the same order of magnitude as the flux of Lyman continuum photons that stars with spectral type B1 or B2 (III) can generate (Panagia 1973). This would in principle be compatible with assuming that the radio continuum emission arises from an ionized region surrounding a hot stellar source associated with the WF IRAS 18043−2116, whose temperature must be $T_\mathrm{eff} > 17\,000$ K, as is the case of hot post-AGB souces (Cerrigone et al. 2008, 2011; Gledhill & Forde 2015). Nevertheless, the FWHM values estimated for the H_2 lines detected in our SINFONI K-band spectrum indicate that the broadening of the line is larger than what could be expected from Doppler shifting in a radiative-excited scenario. In addition, the lack of high-energy H_2 lines, as well as the nondetection of Brγ and He recombination lines also support a shock-excited scenario over the UV-pumped scenario for the H_2 emission. Although the radiative scenario cannot be ruled out, the radio flux is therefore most likely the result of the propagation of a (partially) ionizing shock front, generated by the interaction between a collimated high-velocity outflow and the steadily expanding and relic CSE formed in the AGB phase. The molecular layers swept up by the shock front might be related to those traced by the H_2O maser and H_2 line emission. Nonetheless, regardless of the source of the emission, a turnover frequency, which is a feature rarely observed toward low- and intermediate-initial mass late-type stars, can still be inferred from the JVLA data.

5.3. Velocity field and mass-loss rates

The FWHM of the H_2 lines is consistent with the velocity range covered by the H_2O maser features, where the most blue- and redshifted spectral features appear to move at 132 km s^{-1} and 264 km s^{-1}, respectively, with respect to the systemic velocity of the source (see Fig. 2). If the direction of propagation of the bulk of the shocked gas is not along the line of sight, then the velocity measured for the H_2 and H_2O will be only a fraction of the total velocity of the high-velocity outflow.

Based on the column density derived from the H_2 rotational diagram (Fig. 5), a "mass-loss rate" value can be associated with the H_2 molecular gas component, shock-excited and driven by the passage of a high-velocity outflow ($\dot{M}_{\mathrm{H}_2}$). This value can be estimated using

$$\dot{M}_{\mathrm{H}_2} = 2\mu m_\mathrm{H} N_{\mathrm{H}_2} A \frac{\mathrm{d}v_\mathrm{T}}{\mathrm{d}l_\mathrm{p}}, \quad (2)$$

where μ is the mean atomic weight, m_p is the proton mass, and A is the emitting area, N_{H_2} is the column density, $\mathrm{d}v_\mathrm{T}$ is the tangential component of the velocity vector of the high-velocity outflow, and $\mathrm{d}l_\mathrm{p}$ is the projected length of the emitting region. Because the emitting source is not spatially resolved, the projected length of the emitting region as well as its area are calculated using the seeing of the SINFONI observations, that is, 0.8 arcsec (0.8″ × 10.4 kpc = 8320 AU). Hence, as a function of the distance, $\dot{M}_{\mathrm{H}_2} = 3.8 \times 10^{-9}(D/10.4\ \mathrm{kpc})M_\odot\ \mathrm{yr}^{-1}$. The mass-loss rate estimated from H_2 emission lines would be only representative of the total mass of the molecular component of the circumstellar gas swept up by a collimated high-velocity outflow. Low-luminosity and low-mass young stellar objects are known to display similar features to those observed toward WF nebulae, such as high-velocity, collimated outflows, and shock-excited H_2 emission, which leads to mass-loss rates estimates of between 10^{-10}–10^{-6} $M_\odot$ yr^{-1} (e.g. Garcia Lopez et al. 2013). The $\dot{M}_{\mathrm{H}_2}$ value estimated for the WF IRAS 18043−2116 is within the H_2 mass-loss rate values that are commonly derived for these young stellar objects. The energy input of the mechanism driving their high-velocity molecular outflows might be similar to the case of WF nebulae. However, observational evidence during the early post-AGB phase of (re-)accretion of the material ejected during the AGB phase on the pre-white dwarf star (or on a companion) is crucial to understand whether accretion is related to the generation of the jet-driven winds observed toward WF nebulae.

If this is the case of an inhomogeneous wind, then the mass-loss rate $\dot{M}_\mathrm{ions}$ of ionized gas can be estimated assuming that the photoionization is maintained with the kinetic energy of the wind, this using the ionizing photon rate calculated with Eq. (1), and the hydrogen ionization energy,

$$\dot{N}_\mathrm{i} h\nu = \frac{1}{2}\dot{M}_\mathrm{ions} v^2. \quad (3)$$

In the case of WF IRAS 18043−2116, we have several values related to the outflow velocity (v): the velocity of the most blue- and redshifted spectral features, as well as half the velocity range Δv at FWHM of the different H_2 transition. That is, 132 km s^{-1} and 264 km s^{-1} for the most blue- and redshifted maser spectral features, respectively, and 82 km s^{-1} as half the velocity range covered by the H_2 1–0 S(1) emission at FWHM. Hence, with

v = 132 km s^{-1} and $h\nu$ = 13.6 eV, the mass-loss rate (as a function of the distance) is $\dot{M}_{\rm ions} = 3.3 \times 10^{-5}$ $(D/10.4\ {\rm kpc})$ $M_\odot\,{\rm yr}^{-1}$. Using the LSR velocity of the molecular layers might lead to overstimating $\dot{M}_{\rm ions}$ by not more than one order of magnitude, otherwise the total velocity of the ionized outflow will be >1000 km s^{-1}. In this case, $\dot{M}_{\rm ions}$ should be representative of the ionized gas in the high-velocity outflow. In the case of ionizing winds generating thermal radio continuum emission, Reynolds (1986) concluded that for a given observed radio flux, the mass-loss rate inferred for jet-driven winds is considerable lower than the values estimated when the ionizing winds are assumed to be spherical. According to this, if the radio continuum emission detected is generated by a jet-driven wind, the mass-loss rate derived would be only a reliable upper limit of the ionized gas in the high-velocity outflow.

During the AGB phase, the mass-loss rates estimated from observations are typically in the range between 10^{-8}–10^{-4} $M_\odot\,{\rm yr}^{-1}$, with an average expansion velocity of $v_{\rm exp}$ ~ 15 km s^{-1} (e.g. Schöier et al. 2002; Ramstedt et al. 2008). It is thought that such high mass-loss rates decrease to its minima due to the exhaustion of the hydrogen stellar atmosphere when its mass is $\approx 10^{-2}$ $M_\odot$ (Habing & Olofsson 2003). In the case of the WF IRAS 18043−2116, the velocity field traced by the H_2 lines and H_2O maser emission is one order of magnitude larger than the average velocity measured toward the CSEs of AGB stars. Although the mass-loss rate estimated for the high-velocity outflow and the values reported for the AGB wind are on the same order of magnitude, the velocity field traced by the spectral lines detected (H_2 and H_2O maser) toward the WF IRAS 18043−2116 therefore suggests that the mechanism driving the high-velocity outflow is different from the mechanism driving the relic AGB wind.

Based on the spectral profile and on the full width at zero intensity (FWZI) of ^{12}CO and ^{13}CO lines detected toward a sample of evolved stars (AGBs, post-AGBs, and young planetary nebulae), Sánchez Contreras & Sahai (2012) estimated that the fraction of mass contained in the fastest outflows of their sample (with ^{13}CO FWZI = 160 km s^{-1} and 120 km s^{-1} for IRAS 19374+2359 and IRAS 22036+5306 respectively) are 80% and 55% of the total CSE mass associated with the detected CO emission. This means bipolar structures with mass of 1.0 $M_\odot$ and 0.14 $M_\odot$, respectively. Although the $\dot{M}_{\rm ions}$ values estimated from the radio flux are an upper limit for IRAS 18043−2116 (the ionized outflow might be faster than the molecular layers), fast outflows ($v_{\rm lsr}$ > 100 km s^{-1}) with mass-loss rates on the order of 10^{-6}–10^{-4} $M_\odot$, operating over timescales on the order of the post-AGB phase itself can explain the formation of such high-mass bipolar outflows.

If the WF IRAS 18043−2116 is a post-AGB star, and given the low-mass hydrogen atmosphere of the pre-white dwarf source, the mass in the high-velocity outflows might therefore be fed by a large-scale structure different from the central post-AGB star. The accretion by the central star of the material in a magnetized rotating disk is the most widely accepted scenario for the launching of collimated high-velocity molecular outflows detected toward young stellar objects in a wide mass range. In post-AGB stars, the formation of a rotating disk implies a perturbation on the spherically expanding AGB wind scenario, mostly because the angular momentum of the material ejected from the AGB star is thought to be negligible. The formation of a rotating disk could be well explained by the presence of a (sub-)stellar companion that provides angular momentum to the material ejected by the AGB star (Zijlstra et al. 2006). Disk structures in post-AGB stars have been inferred in most cases from near- and/or far-IR excess of emission as well as from CO line emission, and only a few of them have been spatially resolved with interferometric observations at submillimeter wavelegths (Bujarrabal et al. 2013, 2016). We therefore speculate that a magnetized rotating disk could be the source of mass that feeds the collimated high-velocity outflow. High angular resolution observations at submillimeter wavelengths would test our interpretation.

6. Conclusions

Although the source is not spatially resolved, the results from our multiwavelength observations and the radiative transfer models indicate the following:

- The molecular emission that is detected, that is, the H_2O maser emission and the H_2 ro-vibrational line emission, might be generated in the molecular layers around high-velocity outflows. The high-velocity field traced by the molecular emission highlights the action of a mechanism that drives material with velocities at least one order of magnitude higher than the estimated average velocity field of the AGB wind.
- Given the temporal gap of two years between the measurements of the flux density at 22 GHz taken with ATCA in 2013, and those at lower frequencies (1.5 GHz, 3 GHz, and 5 GHz) performed with JVLA in 2015, the best fits of the radiative transfer models suggest two possible scenarios:
  - Thermal emission with a significant nonthermal (synchrotron) component: in this case, the flux density at 22 GHz is assumed to be constant between 2013 and 2015. The best fit suggests a nonthermal component with $\alpha = -0.7$, and a flux density of 0.15 mJy at 22 GHz. Thus, a nonthermal component could be associated with the most energetic particles interacting with the ionizing shock front, whereas the thermal component could be associated with free particles with lower kinetic temperature at the post-shock region.
  - Thermal emission: Our best fit indicates that if the radio flux is dominated by thermal Bremsstrahlung emission, the flux density at 22 GHz should have increased by about 20% in the period between 2013 and 2015. From the density values retrieved from models that assume only thermal emission, the electron density should have increased by 10% in the two-year period. Such growth of the density of thermal electrons could be associated with the propagation of a (partially) ionizing shock front throughout the slower AGB wind.
- The radio flux at the optically thin regime suggests mass-loss rates on the order of 10^{-5} $M_\odot\,{\rm yr}^{-1}$. Given the exhaustion of material on the stellar atmosphere of the mass-losing star at the end of the AGB phase, we speculate that the outflowing material might be fed by another large-scale structure, for instance, a circumstellar disk. High angular resolution observations are required to confirm the radio flux source and to determine whether the outflowing mass is channeled by (re-)accretion of material from a rotating circumtellar disk into the high-velocity outflow.

The results of our multiwavelength observations support a scenario where the main energy input for the dynamics of large-scale bipolar outflows could be associated with the launching mechanism and the propagation of a thermal radio jet throughout the CSE of the WF IRAS 18043−2116. The detected

ro-vibrational lines of molecular hydrogen, high-velocity spectral features of H_2O maser emission detected at 22 GHz and 321 GHz, with peak flux ratio ≈1 (Tafoya et al. 2014); radio flux at centimeter wavelegths, in addition to the previous reports on the detection OH maser lines, and in particular of the OH 1720 transition (Deacon et al. 2004), show the complexity of the processes going on in the CSE of this WF nebulae.

Acknowledgements. Part of this work is based on observations collected at the European Organisation for Astronomical Research in the Southern Hemisphere under ESO program 095.D-0574(A). The National Radio Astronomy Observatory is a facility of the National Science Foundation operated under cooperative agreement by Associated Universities, Inc. The Australia Telescope Compact Array is part of the Australia Telescope National Facility which is funded by the Australian Government for operation as a National Facility managed by CSIRO. A.F.P.S. aknowledges the Mexican Society of Physics and the National University of Mexico for postdoctoral fellowships during his residence in Mexico. R.G.L. has received funding from the European Union's Horizon 2020 research and innovation programe under the Marie Sklodowska-Curie grant agreement No. 706320. W.V. and D.T. acknowledge support from ERC consolidator grant 614264.

References

Bains, I., Cohen, M., Chapman, J. M., Deacon, R. M., & Redman, M. P. 2009, MNRAS, 397, 1386
Bonnet, H., Abuter, R., Baker, A., et al. 2004, The Messenger, 117, 17
Bujarrabal, V., Castro-Carrizo, A., Alcolea, J., & Sánchez Contreras, C. 2001, A&A, 377, 868
Bujarrabal, V., Alcolea, J., Van Winckel, H., Santander-García, M., & Castro-Carrizo, A. 2013, A&A, 557, A104
Bujarrabal, V., Castro-Carrizo, A., Alcolea, J., et al. 2016, A&A, 593, A92
Cerrigone, L., Umana, G., Trigilio, C., et al. 2008, MNRAS, 390, 363
Cerrigone, L., Trigilio, C., Umana, G., Buemi, C. S., & Leto, P. 2011, MNRAS, 412, 1137
Deacon, R. M., Chapman, J. M., & Green, A. J. 2004, ApJS, 155, 595
Deacon, R. M., Chapman, J. M., Green, A. J., & Sevenster, M. N. 2007, ApJ, 658, 1096
Eisenhauer, F., Schödel, R., Genzel, R., et al. 2003, ApJ, 597, L121
Forde, K. P., & Gledhill, T. M. 2012, MNRAS, 421, L49
Garcia Lopez, R., Caratti o Garatti, A., Weigelt, G., Nisini, B., & Antoniucci, S. 2013, A&A, 552, L2
Gledhill, T. M., & Forde, K. P. 2012, MNRAS, 421, 346
Gledhill, T. M., & Forde, K. P. 2015, MNRAS, 447, 1080
Gómez, J. F., Rizzo, J. R., Suárez, O., et al. 2011, ApJ, 739, L14
Gonidakis, I., Chapman, J. M., Deacon, R. M., & Green, A. J. 2014, MNRAS, 443, 3819
Gray, M. D., Baudry, A., Richards, A. M. S., et al. 2016, MNRAS, 456, 374
Habing, H. J., & Olofsson, H. 2003, Asymptotic giant branch stars (New York, Berlin: Springer)
Hollenbach, D., Elitzur, M., & McKee, C. F. 2013, ApJ, 773, 70
Humphreys, E. M. L. 2007, in Astrophysical Masers and their Environments, eds. J. M. Chapman, & W. A. Baan, IAU Symp., 242, 471
Kurtz, S. 2005, in Massive Star Birth: A Crossroads of Astrophysics, ed. R. Cesaroni, M. Felli, E. Churchwell, & M. Walmsley, IAU Symp., 227, 111
Lagadec, E., Verhoelst, T., Mékarnia, D., et al. 2011, MNRAS, 417, 32
Likkel, L., & Morris, M. 1988, ApJ, 329, 914
Panagia, N. 1973, AJ, 78, 929
Pérez-Sánchez, A. F., Vlemmings, W. H. T., & Chapman, J. M. 2011, MNRAS, 418, 1402
Pérez-Sánchez, A. F., Vlemmings, W. H. T., Tafoya, D., & Chapman, J. M. 2013, MNRAS, 436, L79
Ramstedt, S., Schöier, F. L., Olofsson, H., & Lundgren, A. A. 2008, A&A, 487, 645
Reid, M. J., Schneps, M. H., Moran, J. M., et al. 1988, ApJ, 330, 809
Reid, M. J., Menten, K. M., Zheng, X. W., et al. 2009, ApJ, 700, 137
Reynolds, S. P. 1986, ApJ, 304, 713
Sahai, R., Le Mignant, D., Sánchez Contreras, C., Campbell, R. D., & Chaffee, F. H. 2005a, ApJ, 622, L53
Sahai, R., Sánchez Contreras, C., & Morris, M. 2005b, ApJ, 620, 948
Sánchez Contreras, C., & Sahai, R. 2012, ApJS, 203, 16
Sánchez Contreras, C., Sahai, R., Gil de Paz, A., & Goodrich, R. 2008, ApJS, 179, 166
Sault, R. J., Teuben, P. J., & Wright, M. C. H. 1995, in Astronomical Data Analysis Software and Systems IV, eds. R. A. Shaw, H. E. Payne, & J. J. E. Hayes, ASP Conf. Ser., 77, 433
Schöier, F. L., Ryde, N., & Olofsson, H. 2002, A&A, 391, 577
Schraml, J., & Mezger, P. G. 1969, ApJ, 156, 269
Sevenster, M. N., & Chapman, J. M. 2001, ApJ, 546, L119
Shull, J. M., & Hollenbach, D. J. 1978, ApJ, 220, 525
Tafoya, D., Franco-Hernández, R., Vlemmings, W. H. T., Pérez-Sánchez, A. F., & Garay, G. 2014, A&A, 562, L9
Vlemmings, W. H. T., Diamond, P. J., & Imai, H. 2006, Nature, 440, 58
Walsh, A. J., Breen, S. L., Bains, I., & Vlemmings, W. H. T. 2009, MNRAS, 394, L70
Yung, B. H. K., Nakashima, J.-i., Imai, H., et al. 2011, ApJ, 741, 94
Zijlstra, A., Lagadec, E., Matsuura, M., Chesneau, O., & Etoka, S. 2006, The Messenger, 124